Catal Lett (2017) 147:2987–3003
DOI 10.1007/s10562-017-2188-0

Negative Effects of Dopants on Copper–Ceria Catalysts for CO Preferential Oxidation Under the Presence of CO_2 and H_2O

Jiwoo Oh[1] · Jeong Do Yoo[2] · Keunsoo Kim[3] · Hyung Joong Yun[4] · WooChul Jung[2] · Joongmyeon Bae[1]

Received: 7 July 2017 / Accepted: 7 September 2017 / Published online: 3 October 2017

Abstract The effects of non-reducible dopants on copper–ceria catalysts for the preferential oxidation of carbon monoxide (CO PROX) were experimentally investigated by adding a non-reducible rare-earth element into the ceria support. Gadolinium-doped cerium oxides were synthesized by a combustion method as a support material for the copper–ceria catalytic system. Various compositions of the catalysts, i.e., $CuO/Ce_{1-x}Gd_xO_{2-\delta}$ (x = 0, 0.05, 0.1, 0.13, 0.18, 0.25 and 0.35), were prepared. The physical, structural, redox and surface chemical properties of the prepared catalysts were characterized by inductively coupled plasma mass spectrometry (ICP-MS), N_2 isotherms, X-ray diffraction (XRD), Raman spectroscopy, transmission electron microscopy (TEM), H_2 temperature-programmed reduction (H_2-TPR) and X-ray photoelectron spectroscopy (XPS) analyses. To investigate the influence of the dopants on the CO PROX, an activity test was conducted for each sample under a reactant stream containing CO, H_2, CO_2 and H_2O. Negative effects of the dopants on the CO PROX activity were experimentally observed. Several characteristics on the catalysts induced by the insertion of dopants caused the effects. The presence of the non-reducible dopants on the surface hindered the efficiency of the redox equilibrium between copper and cerium, which is the essential process for CO PROX. Surface oxygen vacancies, generated by the introduction of foreign dopants, were not beneficial to the CO PROX activity. Copper species on the catalysts might be penetrated through these vacancies and protected as non-reactive reduced form in these vacancies.

Electronic supplementary material The online version of this article (doi:10.1007/s10562-017-2188-0) contains supplementary material, which is available to authorized users.

✉ Joongmyeon Bae
jmbae@kaist.ac.kr

[1] Department of Mechanical Engineering, Korea Advanced Institute of Science and Technology, 291 Daehak-ro, Yuseong-gu, Daejeon 34141, Republic of Korea

[2] Department of Materials Science and Engineering, Korea Advanced Institute of Science and Technology, 291 Daehak-ro, Yuseong-gu, Daejeon 34141, Republic of Korea

[3] Department of Mechanical Science and Engineering, University of Illinois at Urbana-Champaign, 1206 West Green Street, Urbana 61801, IL, USA

[4] Advanced Nano Surface Research Group, Korea Basic Science Institute, 169-148 Gwahak-ro, Daejeon 34133, Republic of Korea

Graphical Abstract

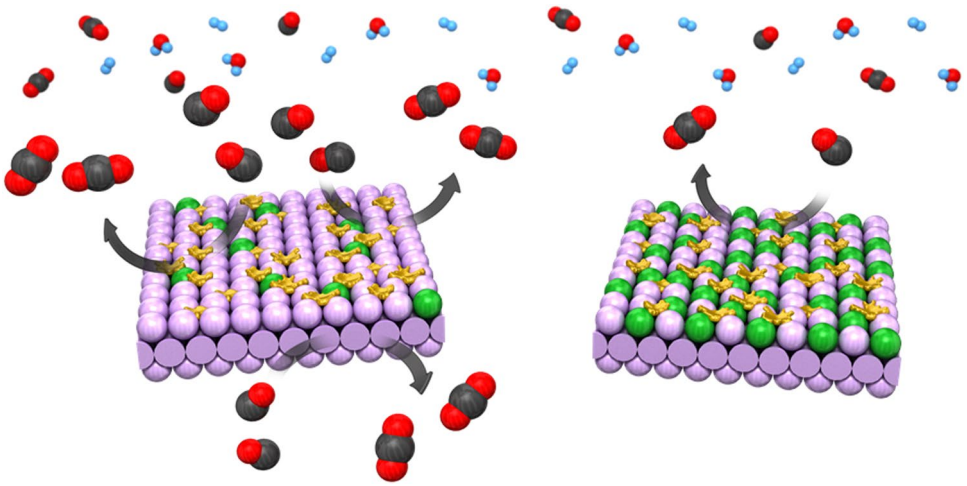

Keywords CO preferential oxidation (CO PROX) · Copper–ceria catalysis · Gd-doped ceria support · Metal–support interaction

1 Introduction

Due to the increased public interest in environmental issues and the need for eco-friendly energy systems, low-temperature proton exchange membrane fuel cell (PEMFC) systems have been widely studied from various perspectives. Most commercial PEMFC systems include reformers to produce hydrogen from conventional hydrocarbon fuels. The reforming components typically contain the main reformer, which is selected among steam reforming, partial oxidation, and autothermal reforming reactions depending on the target application of the system, and a following water gas shift (WGS) reactor is equipped to improve the hydrogen yield [1]. After passing through the WGS reactor, the product mixture contains 40–75 vol.% H_2, 15–25 vol.% CO_2, 10–15 vol.% H_2O, 0.5–2 vol.% CO, and N_2 balance [2]. However, this mixture is not yet usable in fuel cells because of the CO content, which must be diminished to low levels to prevent poisoning the platinum-based anode. Anodes utilizing a bi-metallic alloy can tolerate less than 100 ppm CO in the mixture [3]. Among the applicable CO removal processes, such as CO methanation, pressure swing adsorption (PSA), and CO preferential oxidation (CO PROX), CO PROX is the most appropriate method to remove CO to achieve a desirable level, considering the technical reliability and the size of the system.

Several types of catalysts have been developed for CO PROX, including catalysts based on precious metals, gold and transition metals. Precious-metal-based catalysts, such as Pt [4], Pd [5], Ru [6], and Rh [7], have been studied for a long time. Particularly, platinum-group catalysts have been reviewed since the 1960s and have demonstrated acceptable activities and stabilities in appropriate temperature ranges [4, 8]. However, these catalysts show severe side reactions, such as unwanted hydrogen oxidation and CO_2 methanation for gases containing CO_2 and moisture following their intrinsic reaction mechanism [9, 10]. Gold-based catalysts have also been studied and present desirable activities [11]. Despite their high conversion abilities for CO oxidation, their use is limited because of their high cost and low durability in the presence of moisture. In recent decades, transition-metal-based catalysts, which are relatively more economical than precious-metal- and gold-based catalysts, have been studied, such as catalysts based on Co [12], Cu [13, 14], and Mn [15]. Among these catalysts, CuO/CeO_2 mixed-oxide catalysts have garnered attention for CO PROX due to their excellent performances at desirable temperatures between 100 and 200 °C. The CuO/CeO_2 catalyst system also shows higher selectivity than platinum-group catalysts [16] and is more stable under CO PROX conditions than gold-based catalysts [17].

Many studies have shed light on the origin of the high activity of this CuO/CeO_2 system, which is associated with strong metal-support interactions, as expressed by the redox couple between copper and cerium derived from the following equation [13, 18–20].

$$Ce^{4+} + Cu^{+} \leftrightharpoons Ce^{3+} + Cu^{2+} \quad (1)$$

The correlation between the redox equilibrium and catalytic performance strongly indicated that the CO PROX reaction follows a Mars-van Krevelen type mechanism [21]. Previous researchers have attempted to increase the redox ability by introducing other foreign materials into the ceria lattice. These dopants can enhance the oxygen storage capacity (OSC) of ceria, thus improving the catalytic activity of

the copper–ceria system [17, 22–25]. Wang et al. first tried to include a rare-earth dopant inside the ceria lattice for the CuO/samarium-doped ceria system and evaluated its CO PROX activity [22]. Lin et al. reported a catalyst system with a tin-doped ceria support, which exhibited high CO conversion at low temperature [23]. Chen et al. revealed that incorporating Zr^{4+} into the ceria lattice not only enhanced the oxygen mobility but also provided enhanced catalytic activity [24]. Wu et al. reported that a $CuO/Ce_{0.8}Ti_{0.2}O_2$ catalyst exhibited the best CO PROX performance among other samples with various titanium-doped ceria supports [17]. Recently, Cecilia et al. reported that $CuO/Ce_{0.9}Zr_{0.1}O_2$ showed the best performance among their samples and that catalysts containing rare-earth-doped ceria supports also exhibited better CO conversion abilities than a pure ceria-supported catalyst [25].

Foreign-ion doping into ceria supports has not always provided positive results for CO PROX. Ratnasamy et al. compared CuO/CeO_2, CuO/CeO_2–ZrO_2, and CuO/ZrO_2, fabricated using a co-precipitation method, among which the pure ceria-supported catalyst showed the best performance [26]. This type of inferior catalytic activity generated by Zr^{4+} doping was also reported by Ayastuy et al. [27]. Martinez-Arias tested the CO PROX activity for CuO/Ce–M–O_2 catalysts (M = Zr, Tb) prepared using a reverse micro-emulsion method and reported that the performance was not considerably enhanced by the doping [28]. These inconsistent results concerning the effects of doping foreign ions into ceria may be due to the differences between the types of dopant element used in the various studies.

In this context, the exact role of doping in the ceria support must be revealed by changing the elements and varying the ratio of the dopant. Incorporating rare-earth elements into ceria can enhance its OSC and the mobility of oxygen in the lattice structure [29]. The rare-earth ions in ceria can easily increase the oxygen vacancies in the lattice and surface, and are also known as stabilizers in ceria-based catalytic systems [30, 31]. Gadolinium-doped ceria, $Ce_{1-x}Gd_xO_{2-\delta}$, has been widely used in various applications due to its high OSC and its thermal and electrical stability. This material has been applied as a catalyst by itself or as a support material for mixed metal oxide catalysts in direct CO oxidation [30], hydrogen production from various types of hydrocarbon fuels [32, 33], methyl mercaptan decomposition [34], and solid oxide fuel cells [35]. According to recent reports, rare-earth-doped ceria supports for gold-based catalysts can enhance the OSC and catalytic activity for the WGS [36] and CO PROX [37] processes. However, few studies have explored the relationship between the characteristics and CO PROX activities of copper catalysts supported on gadolinium-doped ceria.

Therefore, in this paper, gadolinium-doped ceria supports with various atomic ratios were prepared to investigate the effect of doping the CuO/CeO_2 catalysts on their characteristics and CO PROX performances. The support materials were synthesized using a combustion method, and the copper contents were physically mounted using an impregnation method. The prepared catalysts were analyzed using various characterization techniques to identify the evident differences in their physical, structural, redox and surface chemical properties. The catalysts were compared under industrial CO PROX conditions simultaneously containing not only H_2 and CO but also CO_2 and H_2O to evaluate the effects of the dopants in the ceria support. Finally, the effects of gadolinium doping will be discussed with the results of the CO PROX activity to conclude the exact role and effect of the foreign dopant.

2 Experimental

2.1 Preparation of the Catalysts

Ceramic oxides, $Ce_{1-x}Gd_xO_{2-\delta}$ (x = 0, 0.05, 0.10, 0.13, 0.18, 0.25 and 0.35), were prepared using the glycine nitrate process (GNP). Both metal nitrate precursors, $Ce(NO_3)_3{\cdot}6H_2O$ and $Gd(NO_3)_3{\cdot}6H_2O$, were supplied by Sigma Aldrich with a purity of 99.9%. For the GNP, the precursors were dissolved in deionized water (>15 MΩ) to achieve the designated molar ratio of cerium to gadolinium ions. To generate the porous support material for the catalyst, glycine was added in an excess amount to the nitrates in solution [38]. The powder resulting from the GNP was calcined in a muffle furnace under static air conditions at 500 °C for 4 h. The final ceramic oxide powders were used as support materials for the catalysts.

The copper in the catalysts was added by incipient wetness impregnation on the ceramic supports. Precisely measured copper nitrate precursor to prepare the catalysts containing 4 wt.% copper was dissolved in deionized water. After impregnation, the powders were dried at 150 °C overnight and calcined at 500 °C for 4 h. The final catalysts were labeled CuO/CeO_2 and CuO/CG_X, where X is the molar doping ratio of gadolinium in the ceria structure.

2.2 Catalyst Characterization

The elemental compositions of the prepared catalysts were measured by inductively coupled plasma mass spectrometry (ICP-MS) using an Agilent ICP-MS 7700S. Before the measurements, the powders were pretreated in ethanol solution with a microwave to generate well-dispersed samples. Nitrogen adsorption/desorption isotherms (N_2 at 77.3 K) were conducted on a TriStar II 3020 from Micromeritics to analyze the Brunauer–Emmett–Teller (BET) surface areas. Prior to the measurements, the

catalysts were degassed at 200 °C over 5 h under vacuum to remove any residual moisture and other volatiles. Powder X-ray diffraction (XRD) patterns were collected on a RIGAKU SmartLab equipped with a symmetric Johansson Ge(111) curved crystal monochromator to strictly show the CuKα_1 radiation. The patterns were recorded in the 2θ range of 10°–90° at a scan speed of 0.5°/min. To match the measured patterns and published data for well-known materials, the crystallography open database (COD) was used, which provided reference data for further analysis [39]. The crystalline size and lattice strain for each catalyst were obtained using the Halder–Wagner method. Moreover, every diffraction pattern was refined using the Rietveld refinement method with the PDXL2 software package (Rigaku, version 2.6.1.2) to obtain the lattice parameters. Raman spectra for the catalysts were obtained using an ARAMIS dispersive Raman spectrometer from Horiba Jobin Yvon with a visible laser of 514 nm. Transmission electron microscopy (TEM) was conducted with an FEI Tecnai F30 S-TWIN transmission electron microscope (300 kV) to confirm the crystal structures and morphologies of the catalysts. The chemical compositions were analyzed using energy-dispersive X-ray spectroscopy (EDS). Hydrogen temperature-programmed reduction (H_2-TPR) analyses were conducted to examine the redox properties of the prepared catalysts using a Micromeritics AutoChem 2920 analyzer. The mass of each sample was approximately 50 mg for each measurement. First, the samples were pretreated under a flow of 5% O_2 in He (50 ml/min) at 300 °C for 1 h, followed by purging with pure Ar (50 ml/min) at the same temperature for the same duration. After cooling to 50 °C, the sample was exposed to 10% H_2 in Ar gas (50 ml/min) for 30 min. Finally, the samples were heated to 700 °C at a rate of 10 °C/min with the same hydrogen composition. The amount of consumed hydrogen was measured using a thermal conductivity detector (TCD) and was calibrated using pure CuO as a reference (Sigma Aldrich). X-ray photoelectron spectroscopy (XPS; K-alpha, Thermo Scientific Inc.) with a monochromatic Al-Kα (1486.6 eV) excitation source was employed to investigate the chemical bonding nature of species (C 1s, O 1s, Cu 2p and Ce 3d) in the sample (base pressure: 1×10^{-9} Torr). To minimize the artificial effect on the fresh catalysts by the X-ray during the analysis, we strictly used the monochromatic excitation source. The binding energies of the XPS spectra were calibrated by the position of C 1s (284.6 eV) of adventitious carbon in the air. High-resolution XPS spectra were obtained using an analysis area of 400 µm using a 40 eV pass energy. The deconvolution of the XPS data was performed using CASAXPS software (Version 2.3.16. U.K) by fitting Gaussian–Lorentzian line shapes after subtracting the background by the Shirley method.

2.3 Activity Tests for the Prepared Catalysts

The catalytic performances of the prepared samples were evaluated in a fixed bed reactor installed in a jacket furnace to maintain a constant temperature. All test experiments were conducted at atmospheric pressure and within a temperature range from ambient to 200 °C for dry experiments and from 100 to 250 °C for experiments containing moisture in the reactant mixture. To simulate the reactant mixture, each gas component, including hydrogen, carbon monoxide, carbon dioxide, oxygen and nitrogen, was injected using independent mass flow controllers (MFCs). All gases were of analytical grade from a commercial supplier in South Korea. The water content inside the reactant mixture was supplied using a high-performance liquid chromatography (HPLC) pump (PrimeLine™) and was completely evaporated through a high-temperature sand bath before the reactor. The reactor consisted of a 0.25-inch quartz tube, and two k-type thermocouples were located inside the reactor on the top and bottom of the catalyst bed. All flow lines connected to the reactor were completely sealed with Swagelok tube fittings. The catalyst bed was placed on a glass wool support and located in the isothermal zone of the furnace (5–6 cm). The prepared catalysts were crushed to obtain fine granules with a particle size from 500 to 850 µm. For each experiment, the mass of the catalyst was controlled to be 350 mg, and the total flow rate of the gas mixture was fixed at 50 ml/min to lock the gas hourly space velocity (GHSV) at a single value. The composition of the reactant mixture was varied for different experimental conditions. To evaluate the industrial CO PROX ability, a mixture representing the conventional tail gas of a WGS reactor was used, consisting of 1.0% CO (by volume, hereafter), 1.0% O_2, 50% H_2, 15% CO_2, 10% H_2O and N_2 balance. To investigate the oxidation abilities of the prepared samples, the oxygen contents inside the reactant were varied, as represented by λ values of 1, 2 and 4, defined as the amount of oxygen relative to CO inside the reactant mixture:

$$\lambda = \frac{2 \times [O_2]_{in}}{[CO_2]_{in}} \tag{2}$$

Furthermore, dry CO PROX experiments were conducted because moisture content inside the reactant is known to inhibit CO removal [40]. The reactant mixture was prepared with the same composition as the complete CO PROX conditions excluding H_2O.

At every experimental point, the catalysts were stabilized for 1 h before performing the measurements. The effluent gases were analyzed using an Agilent 490 micro GC system. Two different channels with independent TCDs were equipped. Two columns with Molsieve 5A to

separate CO from O_2 and Polar Plot Q to detect CO_2 at the ppm level were also prepared on the micro GC system. The moisture contents inside the product were completely removed through an absorbent tube. After the measurements, the CO and oxygen conversion rates were calculated using Eqs. (3) and (4), respectively. The oxygen selectivity to CO_2 was calculated using Eq. (5).

$$\text{CO conversion } (X_{CO}) = \frac{[CO]_{in} - [CO]_{out}}{[CO]_{in}} \times 100\ (\%) \quad (3)$$

$$O_2 \text{ conversion } (X_{O_2}) = \frac{[O_2]_{in} - [O_2]_{out}}{[O_2]_{in}} \times 100\ (\%) \quad (4)$$

$$O_2 \text{ selectivity to } CO_2 (S_{CO_2}) = \frac{[CO]_{in} - [CO]_{out}}{2 \times ([O_2]_{in} - [O_2]_{out})} \times 100\ (\%) \quad (5)$$

3 Results and Discussion

3.1 Elemental Composition Analysis

The precise elemental compositions of the prepared catalysts were examined by ICP-MS analysis. The results obtained for all samples are provided in Table 1. The atomic percentage of gadolinium was gradually increased in the prepared catalysts. Furthermore, the copper content in the catalysts was controlled to 4 wt.% within a standard error of 0.09.

3.2 Physisorption Analysis

The nitrogen adsorption/desorption isotherms of the prepared catalysts are provided in Fig. S1. The plots from the catalysts with different supports show similar isotherm trends. Each plot exhibits a steep increase in adsorption at a high relative pressure, which represents the filling of the mesopores on the sample surfaces [41]. Numerical surface properties, such as the BET surface area (S_{BET}), average pore size and total pore volume, of the samples were also calculated from the N_2 isotherm data and are presented in Table 1. The average pore sizes of the samples are within the range of 7.58–8.93 nm, and the average pore volume is 0.113 cm^3/g. The pore sizes and volumes seem to decrease upon increasing the amount of dopant, but big differences were not found among the data. The S_{BET} values are also similar for all the prepared catalysts with an acceptable standard deviation. These findings suggest that the prepared samples have similar physical adsorption ability for catalysis.

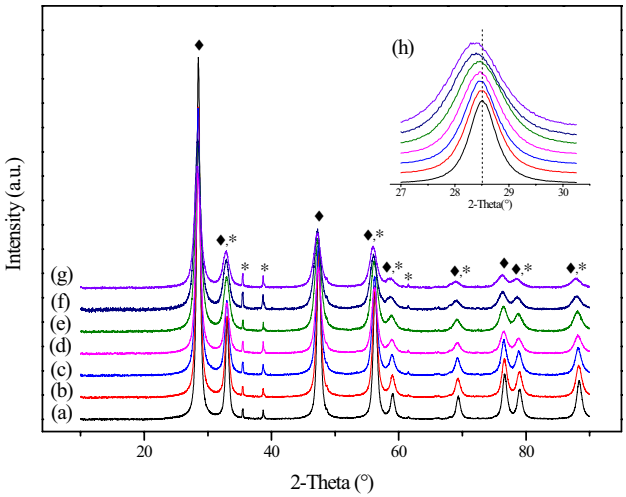

Fig. 1 XRD patterns for the prepared catalysts: (*a*) CuO/CeO_2, (*b*) $CuO/CG_{0.05}$, (*c*) $CuO/CG_{0.1}$, (*d*) $CuO/CG_{0.13}$, (*e*) $CuO/CG_{0.18}$, (*f*) $CuO/CG_{0.25}$, and (*g*) $CuO/CG_{0.35}$. The diamonds (filled diamond) indicate the peaks of the ceria support, and the asterisks (*) indicate the peaks of copper oxide. The inset plot (*h*) shows a selected region presenting marginal shifts in the ceria (111) peak to a lower angle

Table 1 Elemental compositions from ICP-MS analysis and surface properties from N_2 isotherm analysis

Label	Catalyst	Cu (wt.%)	Ce (at.%)	Gd (at.%)	S_{BET} (m^2/g)	Average pore size (nm)	Pore volume (cm^3/g)
CuO/CeO_2	CuO/CeO_2	4.3	100.0	0.0	35.833	8.93	0.117
$CuO/CG_{0.05}$	$CuO/CeGd_{0.05}O_{2-\delta}$	4.8	95.5	4.5	38.177	8.24	0.117
$CuO/CG_{0.1}$	$CuO/CeGd_{0.10}O_{2-\delta}$	4.4	91.1	8.9	41.188	7.84	0.118
$CuO/CG_{0.13}$	$CuO/CeGd_{0.13}O_{2-\delta}$	4.6	87.3	12.7	33.300	8.75	0.106
$CuO/CG_{0.18}$	$CuO/CeGd_{0.18}O_{2-\delta}$	4.9	82.3	17.7	39.360	7.96	0.116
$CuO/CG_{0.25}$	$CuO/CeGd_{0.25}O_{2-\delta}$	4.8	74.2	25.8	36.161	7.65	0.107
$CuO/CG_{0.35}$	$CuO/CeGd_{0.35}O_{2-\delta}$	4.3	65.3	34.7	36.454	7.58	0.109
Average					37.287	8.23	0.113
Standard deviation					2.252	0.51	0.005

3.3 Structural Analysis

The XRD patterns of the samples are presented in Fig. 1. In each XRD profile, a typical ceria diffraction pattern is predominantly observed, and the peaks correspond to the well-known fluorite cubic structure of cerium oxide. The absence of secondary peaks, such as Gd_2O_3 on the surface, suggests that the aliovalent gadolinium ions have successfully substituted cerium ions in the lattice and/or that the extracted gadolinium oxides are highly dispersed on top of ceria [30]. In contrast, copper oxide peaks are clearly observed and are marked by asterisks in Fig. 1. These peaks are assigned to the monoclinic tenorite structure of CuO [27]. The presence of these peaks indicates that copper oxide successfully constructs its own structure on the surface of the support. This phenomenon clearly demonstrates that copper was physically mounted on the ceria supports using the impregnation method without an excessive high-temperature calcination [27]. Other copper species, such as Cu_2O and metallic Cu, were not found in the diffraction patterns. However, affirming that all the impregnated copper on the catalysts is in the form of CuO is difficult. Instead, other copper species may exist in undetectable amounts of clusters or highly dispersed structures on the ceria template.

The inset plot in Fig. 1 shows the patterns within a selected 2θ region from 27° to 30° containing the (111) facet peak of the catalyst support. All the data in the inset plot were normalized to clearly compare the patterns. The (111) peak of the samples gradually shifted to a lower angle as the doping amount increased. Previous studies have indicated that the difference between the effective ionic radii of Gd^{3+} and Ce^{4+} causes this shift [42, 43]. According to the work of Shannon, the radius of gadolinium ($r_{Gd^{3+}} = 1.053$ Å) is larger than that of cerium ($r_{Ce^{4+}} = 0.97$ Å) [44]. Normally, larger foreign ions inside the ceria structure relax the lattice, which is reflected in the XRD pattern by a shift in the (111) peak to a lower angle [45].

To elucidate the structural parameters of the catalysts, Rietveld refinements were conducted on the patterns. Table 2 shows several parameters obtained by the Rietveld analysis. The typical refined patterns for all the catalysts are shown in Fig. S2. Along with the observations in the inset plot in Fig. 1, the lattice parameter for the ceria support gradually increased when the doping ratio was increased. The Halder–Wagner method was introduced to calculate the lattice strain (ε) using structural parameters derived from the Rietveld analysis [46]. Table 2 shows the calculated lattice strain values for the catalysts. As the doping amount increased, the ceria lattice strain also gradually increased, indicating that the increased amount of gadolinium likely generated more lattice defects. The lattice strain inside ceria is normally related to the bulk and surface OSC and the possible use of the material as an oxidation catalyst [47]. These oxygen vacancies generated by the addition of dopants and the PROX activity for the catalysts will be discussed in a later section. However, no lattice strain was determined in the copper oxides via calculations, indicating that CuO constructs its own structure on the ceria surface without any intervention [48]. The crystallite sizes of ceria and CuO gradually decreased when the gadolinium doping amount increased, indicating that the particle size of CuO on the surface may follow the size of the ceria template. Therefore, we conclude that the amount of gadolinium in the lattice may determine the final crystallite size of copper oxide on the surface, which also agrees with previously reported results [49].

Raman spectroscopy is an effective optical technique to investigate the structural characteristics of ceramics because of its sensitivity to lattice defects inside the material [50]. The Raman spectra for all the prepared catalysts are

Table 2 Structural parameters of the prepared catalysts

Sample	χ^2	Lattice parameter a of ceria (Å)	Lattice strain of ceria (%)	d-spacing of ceria (Å)[a, c]	Crystallite size of ceria (nm)	d-spacing of CuO (Å)[b, c]	Crystallite size of CuO (nm)
CuO/CeO_2	0.6046	5.4151	0.27	3.127 (3.13)	11.0	2.753 (2.70)	9.2
$CuO/CG_{0.05}$	0.4809	5.4185	0.33	3.127 (3.11)	8.6	2.751 (2.70)	8.3
$CuO/CG_{0.1}$	0.5252	5.4229	0.36	3.131 (3.13)	8.9	2.754 (2.73)	7.7
$CuO/CG_{0.13}$	0.4403	5.4247	0.37	3.133 (3.15)	8.0	2.753 (2.73)	7.2
$CuO/CG_{0.18}$	0.4303	5.4287	0.41	3.135 (3.15)	7.1	2.753 (2.73)	5.8
$CuO/CG_{0.25}$	0.5051	5.4354	0.60	3.140 (3.14)	6.5	2.754 (2.71)	5.6
$CuO/CG_{0.35}$	0.3786	5.4379	0.70	3.142 (3.13)	6.1	2.753 (2.75)	5.3

The parameters of the catalyst support and copper oxide are separately calculated from the Rietveld refinement

[a]Values in this column indicate the d-spacings of the ceria support (111) facets

[b]Values in this column indicate the d-spacings of the CuO (110) facets

[c]Values in parentheses are the measured d-spacings from the TEM images

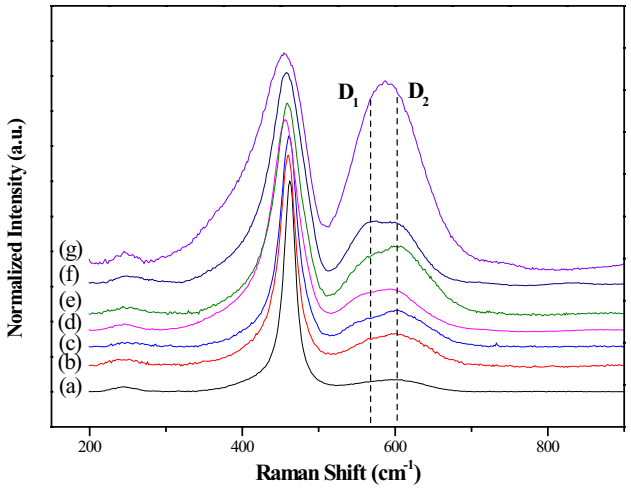

Fig. 2 Raman spectra for all the prepared samples: (*a*) CuO/CeO_2, (*b*) $CuO/CG_{0.05}$, (*c*) $CuO/CG_{0.1}$, (*d*) $CuO/CG_{0.13}$, (*e*) $CuO/CG_{0.18}$, (*f*) $CuO/CG_{0.25}$, and (*g*) $CuO/CG_{0.35}$

presented in Fig. 2. The spectra were obtained in the wavelength range from 200 to 900 cm^{-1} using a visible 514 nm laser. According to previous literature, this visible Raman range is appropriate to observe ceria's typical F_{2g} degenerate band at 464 cm^{-1} and the lattice disorder band, i.e., the D band for lattice defects, near 600 cm^{-1} [51]. Each spectrum shows a clear F_{2g} band at approximately 460 cm^{-1}, and some spectra exhibit a slight offset from the center due to the introduction of the Gd dopant. The F_{2g} bands reveal that the main crystalline structures of the prepared catalysts are fluorite cubic structures, which is consistent with the XRD analysis [52]. Overall, the D band intensity increased with an increasing amount of Gd. This observation agrees well with the trend in the lattice strain derived from the XRD analysis. According to notation from the literature, the D band consists of two different bands, marked D_1 and D_2 in Fig. 2 [51, 53]. First, the D_1 band located at approximately 570 cm^{-1} indicates that lattice defects were generated by extrinsic oxygen vacancies. The D_2 band near 600 cm^{-1} represents defects caused by intrinsic oxygen vacancies [54]. Generally, the intrinsic vacancies in the ceria structure are created by thermal disorder and the presence of Ce^{3+} ions, while the extrinsic vacancies are generated by the introduction of aliovalent ions into the lattice, such as Gd^{3+} ions in this case, and charge compensation effects [50, 55]. According to Taniguchi et al., the intensity ratio between the D_1 and D_2 band reveals the relative concentration between the two types of oxygen defects inside the lattice [51]. As clearly shown in Fig. 2, the relative intensity of the D_1 band compared with that of D_2 increased as the amount of gadolinium increased. Moreover, this phenomenon indicates that the dominant type of oxygen vacancies inside the ceria lattice changed as the gadolinium doping amount increased. Intrinsic oxygen vacancies were predominant among the catalysts with low doping contents, whereas extrinsic oxygen vacancies were more prevalent when the gadolinium content increased.

To finalize the structural analysis, the surfaces of the catalysts were visually examined using TEM. Figure 3 shows the TEM images and the corresponding selected area electron diffraction (SAED) patterns and EDS mapping images of selected catalysts. Detailed information for each image is provided in the caption of Fig. 3. The remaining TEM images and corresponding data are presented in Fig. S3. The surface morphologies of all catalysts are visually similar, regardless of the doping ratio. The SAED patterns, which are presented on the top left of (a) and (c) in Fig. 3, are indexed to the fluorite structure, in agreement with the XRD results [56]. The visibility of the rings becomes faint as the amount of gadolinium increased. In each image, the cerianite (111) and tenorite (110) planes were separately detected by measuring the crystal spacing (d-spacing) [48]. Associated with the XRD results, other copper species, such as Cu_2O or reduced copper, were not visually detected on the surfaces. Table 2 shows the d-spacing values from the XRD analysis and TEM images. A slight increment was observed for the series of d-spacings for ceria (111). This finding is related to the relaxation effect caused by foreign gadolinium inside the ceria lattice [17]. The images in Fig. 3f show the EDS mappings of cerium, gadolinium and copper elements on the representative catalyst, $CuO/CG_{0.1}$. These images confirm that each element was highly dispersed on the surface.

3.4 Redox Analysis

H_2-TPR analysis was conducted to study the redox properties of the samples and to examine the effect of the extrinsic oxygen vacancies on the reducibility of the catalysts. Figure 4 shows the typical H_2-TPR profiles for the samples. The plots in Fig. 4 follow the typical reduction pattern for the copper–ceria system, which has been previously reported in the literature [57]. The overall reduction patterns of the prepared samples clearly appear in a relatively lower temperature region than the patterns for pure ceria [58] and CuO [59]. Ayastuy et al. showed that the presence of copper oxide on the ceria support can enhance the overall reducibility of the catalyst, which is related to the strong metal–support interactions [60]. Furthermore, most profiles notably exhibit more than one reduction peak rather than a single broad peak, unlike that of pure copper oxide. This finding supports the existence of more than one reducible copper and/or copper oxide species on the surface of the prepared catalysts, generated by the interaction with support [10]. Although additional reducible copper oxide species, except CuO, were not found by the structural analysis, a small amount or highly dispersed reducible copper species existed on the surface of the catalysts.

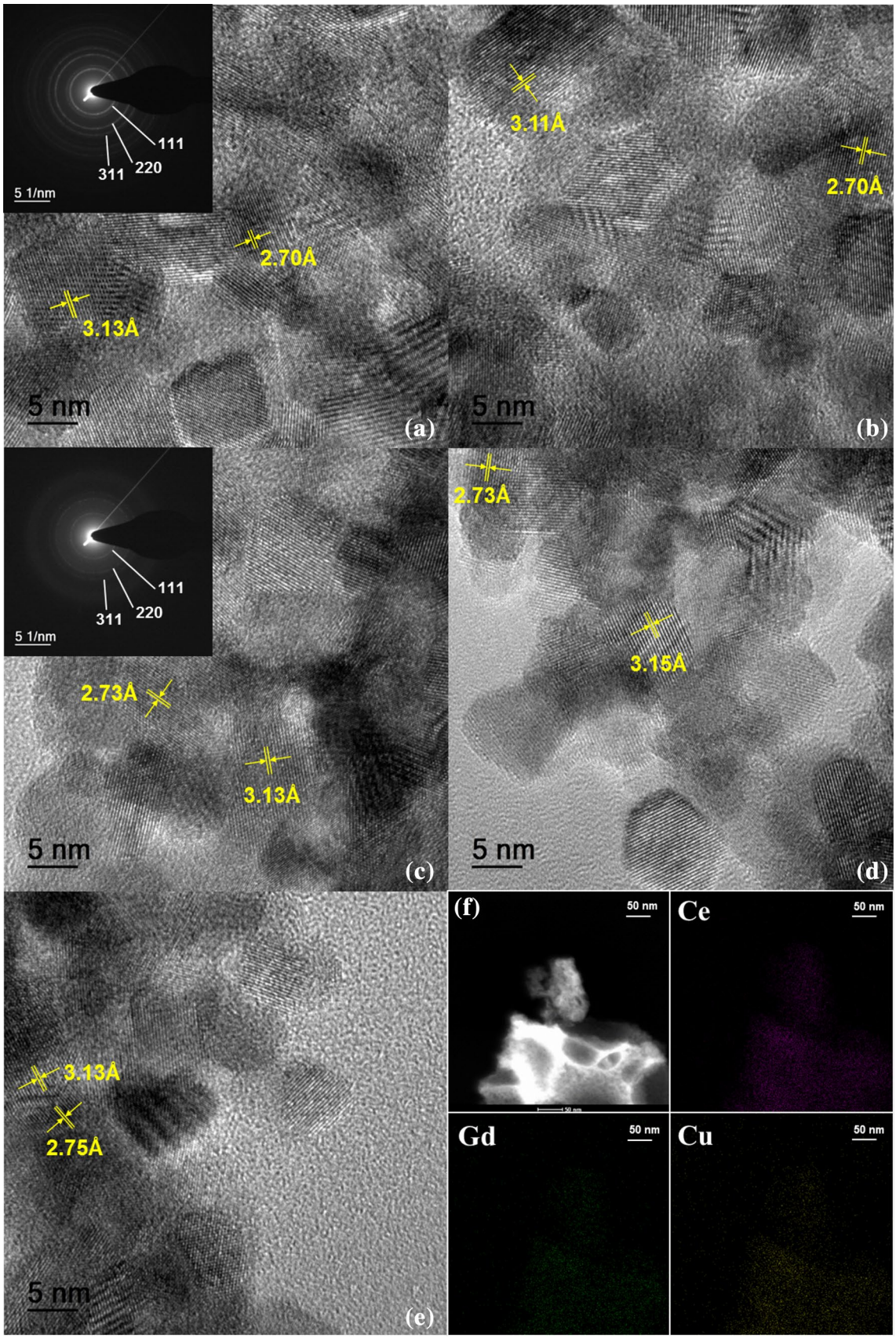
111
311
220
5 1/nm
2.70Å
3.13Å
5 nm
(a)
3.11Å
2.70Å
5 nm
(b)
111
311
220
5 1/nm
2.73Å
3.13Å
5 nm
(c)
2.73Å
3.15Å
5 nm
(d)
3.13Å
2.75Å
5 nm
(e)
(f)
50 nm
Ce
50 nm
Gd
50 nm
Cu
50 nm

◂**Fig. 3** TEM images and corresponding SAED patterns for **a** CuO/CeO_2, **b** CuO/$CG_{0.05}$, **c** CuO/$CG_{0.1}$, **d** CuO/$CG_{0.18}$, and **e** CuO/$CG_{0.35}$. EDS mapping images of the **f** CuO/$CG_{0.1}$ sample and the constituent elements Ce, Gd, and Cu

Figure 4 is divided into three groups based on the similarity of the profiles. The profiles of (a) CuO/CeO_2, (b) CuO/$CG_{0.05}$, and (c) CuO/$CG_{0.1}$ display similar reduction patterns with three distinct peaks between 100 and 230 °C, which are merged in Fig. 4A. Figure 4B shows the profiles of (d) CuO/$CG_{0.13}$ and (e) CuO/$CG_{0.18}$. These profiles display three ambiguous but separable peaks from 150 to 250 °C. Finally, the reduction patterns for (f) CuO/$CG_{0.25}$ and (g) CuO/$CG_{0.35}$ are presented in Fig. 4C, displaying a sharp peak near 250 °C and a broad shoulder on the right side of the peak that persists up to 600 °C. The profiles of the three catalysts in Fig. 4A display the shape of a typical reduction pattern for the copper–ceria system, as previously reported [10, 60–64]. The types of reducible copper species that are present on the catalyst can be confirmed based on these patterns. Various researchers, such as Avgouropoulos [10], Liu [62], Kundakovic [63], and Luo [64], have described the typical reduction pattern of copper–ceria catalysts, consisting of three peaks, so-called peak α, peak β, and peak γ based on the temperature. Peak α, which occurs at the lowest reduction temperature, is associated with finely dispersed CuO with a close interaction with ceria. The second peak β is a well-known indicator of "bulk-like" CuO particles that weakly interact with the ceria support. Peak γ is located at the highest reduction temperature and is related to bulk CuO with larger particles without the interaction with ceria. Pintar et al. also performed rigorous TPR, TPD and TPO analyses of the copper–ceria catalysts. The authors found that the dominant reduction process at peak α is the partial reduction of Cu^{2+}–Cu^{+} and that the main reaction at peak β corresponds to the partial reduction of Cu^{+}–Cu^{0} [61]. All the profiles in Fig. 4A show distinct peaks α, β and γ, and each peak represents three different types of copper species, in accordance with the aforementioned papers. The reduction temperatures for each sample and peaks are presented in Table 3. Sample (a) shows the lowest reduction temperature and exhibits the highest reducibility among the samples. The reduction temperature of each peak gradually increases as the doping ratio is increased. The shifting and merging trend of the peaks are clearly presented in the profiles shown in Fig. 4B. Peak β of sample (d) shifted to the higher temperature region and began to merge with peak γ. Based on the aforementioned studies, this change is attributed to an increased number of copper species that no longer interact with surface ceria. This tendency persists for sample (e), where peak β is barely separated from peak γ. Wu et al. also found that peak β shifted to a higher temperature and merged with peak γ as the Ti doping ratio was increased [17]. Therefore, this tendency seems to be related to the gadolinium content inside the ceria support.

Figure 4C shows the profiles for the remaining samples (f) and (g). The profiles show completely different patterns than those of the other six samples. Peaks α and β are not observed on these profiles. Thus, these samples do not preferentially form the dispersed copper species with a strong interaction with the surface ceria. Instead, the profiles exhibit a sharp single peak at 235 °C for sample (f) and 246 °C for sample (g). The shape of these peaks are fairly similar to the pattern of pure bulk CuO [59]. Therefore, these peaks correspond to peak γ for samples (f) and (g), indicating the presence of bulk CuO clusters that do not interact with surface ceria. The copper species on samples (f) and (g) may have fully oxidized in the pretreatment step before the TPR analysis, as no interactions exist to prevent the full oxidation of the copper species. Another broad shoulder appears on the right side of the single peak in both profiles. This broad shoulder persists up to 600 °C. Therefore, this shoulder may correspond to the reduction of the ceria support, which is no longer interacts with copper on the surface. This observation suggests that the broad shoulders in Fig. 4C, can be labeled as a new peak (peak δ) and are assigned to the reduction of ceria support, indicating the separation of copper and ceria.

Table 3 shows the maximum temperature of each peak. The reduction temperatures for peak α, β, and γ gradually shifted to higher temperatures when the doping ratio increased. These shifts indicate that the interaction between copper on the top and surface ceria gradually weakened as the gadolinium content increased. However, peaks α and β disappeared when the gadolinium loading exceeded an atomic ratio of 0.2. Furthermore, the new broad shoulder peak, δ, appeared as an indicator of the separation between the surface copper species and ceria. Table 3 also shows the relative intensities of peaks α, β, and γ. The values are normalized to the intensity of peak β. As the doping ratio increased, the intensity of peak α gradually decreased, similar to the shift of the reduction temperature. Furthermore, the relative intensity of peak γ gradually increased, alluding a weakened interaction between copper and ceria.

3.5 Surface Electronic Analysis

To determine the effects of the dopants on the catalyst surfaces, XPS was used to analyze the surface chemical compositions. Table 4 contains the chemical compositions of the catalyst surfaces expressed by the relative atomic ratio between the copper and rare-earth elements. The relative copper ratio on the surface gradually decreased when the gadolinium doping ratio increased, which is in obvious contrast to the elemental analysis results in Table 1. This difference of the chemical composition between the bulk and surface of the catalyst corresponds to a "metal-burial"

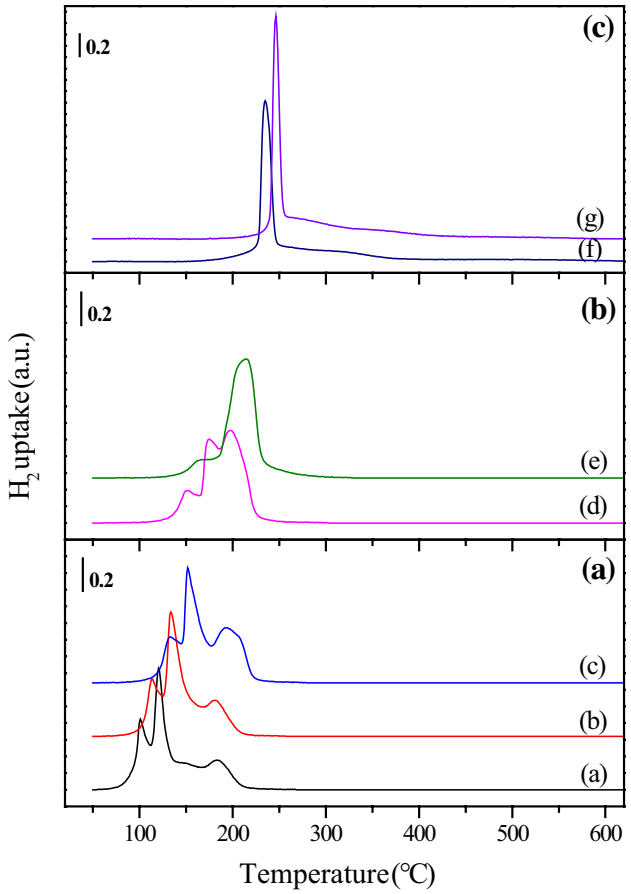

Fig. 4 H_2-TPR profiles for (*a*) CuO/CeO_2, (*b*) $CuO/CG_{0.05}$, (*c*) $CuO/CG_{0.1}$, (*d*) $CuO/CG_{0.13}$ (*e*) $CuO/CG_{0.18}$, (*f*) $CuO/CG_{0.25}$, and (*g*) $CuO/CG_{0.35}$

Table 3 H_2-TPR analysis of the prepared catalysts

Sample	T_α (°C)	T_β (°C)	T_γ (°C)	T_δ (°C)	Intensity[a] I_α:I_β:I_γ
CuO/CeO_2	103.0	120.6	173.4	–	0.58:1.00:0.24
$CuO/CG_{0.05}$	113.3	133.5	181.0	–	0.46:1.00:0.29
$CuO/CG_{0.1}$	137.1	153.2	198.2	–	0.40:1.00:0.48
$CuO/CG_{0.13}$	151.2	173.5	198.7	–	0.38:1.00:1.11
$CuO/CG_{0.18}$	166.4	205.6	216.5	–	0.17:1.00:1.07
$CuO/CG_{0.25}$	–	–	235.3	258.2	–
$CuO/CG_{0.35}$	–	–	246.1	276.2	–

[a]Ratio of the intensities of peaks α, β, and γ normalized to the intensity of peak β at a maximum temperature

effect on doped ceria. According to previous literature, small metal atoms, such as copper in this case, can penetrate the ceria lattice through the surface and bulk oxygen vacancies [65]. As the amount of gadolinium dopants increases, a higher number of surface and bulk oxygen vacancies are likely generated and copper elements on the surface are likely to be buried through the vacancies.

Table 4 Chemical composition analysis of the catalyst surfaces

Sample	Cu/(Ce + Gd)[a]	Ce^{3+} (%)	Cu^{2+}/(Cu^+ or Cu^0)
CuO/CeO_2	0.325	15.3	2.51
$CuO/CG_{0.05}$	0.345	14.6	2.59
$CuO/CG_{0.1}$	0.315	13.4	1.78
$CuO/CG_{0.13}$	0.247	12.5	1.55
$CuO/CG_{0.18}$	0.189	12.4	1.35
$CuO/CG_{0.25}$	0.158	12.6	0.84
$CuO/CG_{0.35}$	0.151	12.7	1.05

[a]Relative atomic ratio was calculated by the surface chemical composition data from the XPS analysis

Figure 5 shows the measured XPS spectra of the Ce 3d core level and the deconvoluted results of all the samples. Previous studies have reported detailed descriptions of the XPS core level spectra of Ce^{4+} and Ce^{3+} for CeO_2 and Ce_2O_3, respectively. Moreover, the Ce 3d core level contains various peaks due to hybridization between the Ce 4f levels and the O 2p levels [66, 67]. The deconvoluted peaks indicated by the dashed lines in Fig. 5 correspond to Ce^{3+} components (Ce $3d^9$ $4f^1$ O $2p^6$). The amount of Ce^{3+} relative to the amount of both Ce^{4+} and Ce^{3+} was quantified using the following formula:

$$Ce^{3+}(\%) = \frac{S(Ce^{3+})}{S(Ce^{3+} + Ce^{4+})} \times 100 \quad (6)$$

where S(x) represents the area of the deconvoluted peak assigned to a component.

Table 4 contains the calculated Ce^{3+} ratios of the samples. The deconvolution of the Ce 3d core level spectra shows the coexistence of both 3+ and 4+ species, and the amount of Ce^{3+} is below 16% in all cases. All XPS calculations inevitably assumed that the ratio of chemical states is spatially constant within the sample. Therefore, the real percentages with regard to spatial variations of the atomic ratio of the Ce^{3+} and Ce^{4+} ions in the sample may show slight deviations from the calculated results. The portion of Ce^{3+} gradually decreased in the catalysts as the doping ratio increased. This calculation result suggests that the amount of reducible ceric atoms decreased as the amount of non-reducible dopants increased. The chemical composition of the bulk ceramic around the cerium and gadolinium is also represented on the surface of the catalysts. Therefore, the bulk oxygen vacancies confirmed by the structural analysis may also be present on the surface of the catalysts as surface oxygen vacancies. Notably, the decrease of the Ce^{3+} ratio is related to a decrease of the

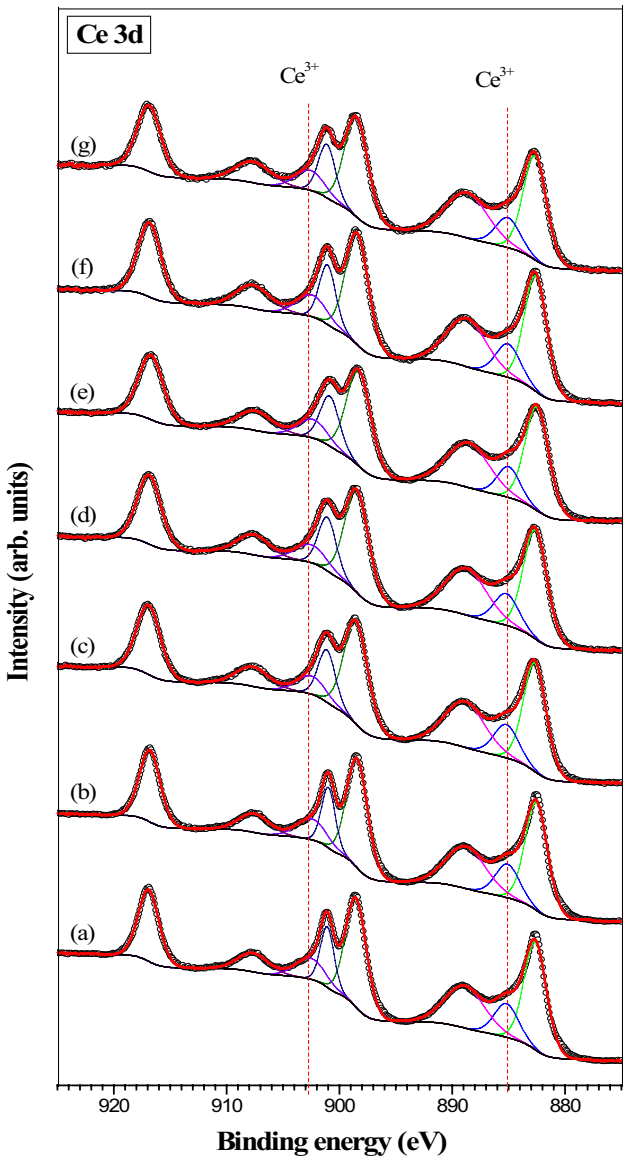

Fig. 5 Measured and deconvoluted Ce 3d XPS peaks of the samples: (*a*) CuO/CeO_2, (*b*) $CuO/CG_{0.05}$, (*c*) $CuO/CG_{0.1}$, (*d*) $CuO/CG_{0.13}$, (*e*) $CuO/CG_{0.18}$, (*f*) $CuO/CG_{0.25}$ and (*g*) $CuO/CG_{0.35}$

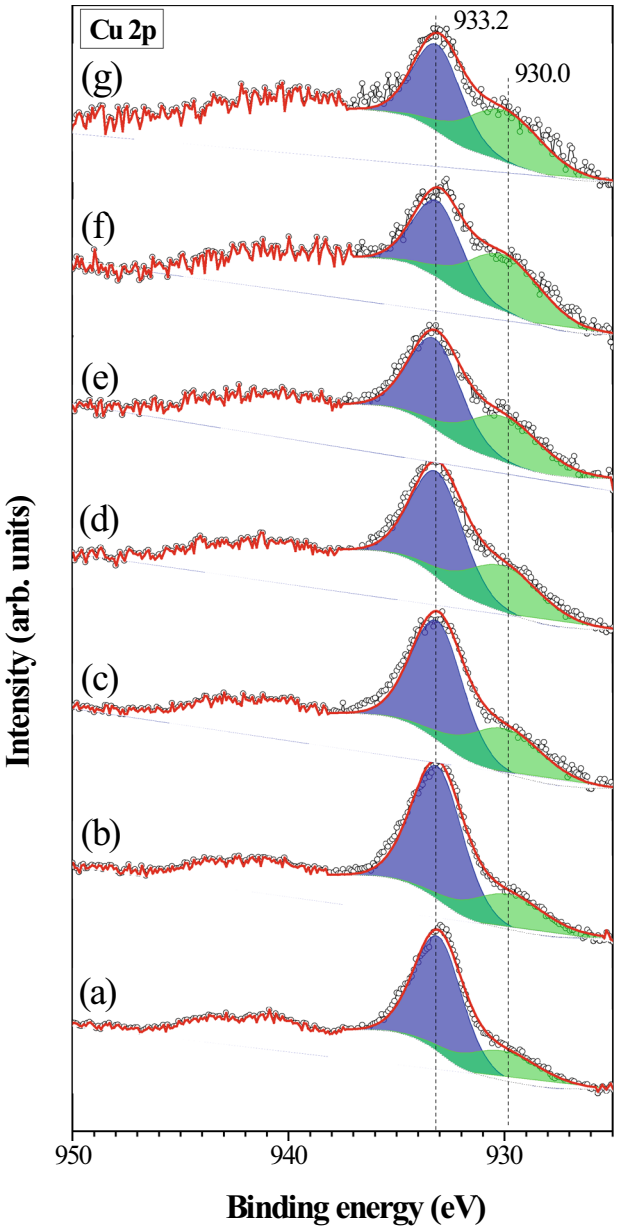

Fig. 6 Measured and deconvoluted Cu 2p XPS peaks of the samples: (*a*) CuO/CeO_2, (*b*) $CuO/CG_{0.05}$, (*c*) $CuO/CG_{0.1}$, (*d*) $CuO/CG_{0.13}$, (*e*) $CuO/CG_{0.18}$, (*f*) $CuO/CG_{0.25}$ and (*g*) $CuO/CG_{0.35}$

strong metal–support interaction with the surface copper species, as confirmed by the TPR results, which may affect the PROX activities of the catalysts.

The Cu 2p XPS spectra for the samples are shown in Fig. 6. Two major XPS peaks for different types of copper species are clearly distinguishable. The higher Cu $2p_{3/2}$ binding energy at 933.2 eV along with the satellite peaks, located approximately between 938 and 948 eV, usually corresponds to Cu^{2+} species in the form of CuO [68]. The lower Cu $2p_{3/2}$ binding energy at 930.0 eV without the presence of satellite peaks represents the existence of reduced copper species, such as Cu^+ and Cu^0, on the surface [69]. Interestingly, the lower binding energy signal of the Cu $2p_{3/2}$ main peak gradually increased as the gadolinium doping ratio increased. Additionally, the satellite peaks corresponding to Cu^{2+} species greatly decreased as the doping amount increased. Table 4 contains the relative ratios of $Cu^{2+}/(Cu^+$ or $Cu^0)$, clearly showing the increasing trend of reduced copper species. This trend indicates that the reduced copper species are dispersed and maintained on the surface of catalysts, which have a large number of gadolinium dopants, even in the oxidative environment. This phenomenon can be explained by the concept of "metal-nesting" [65]. If a sufficient number of surface oxygen vacancies exist, physically

mounted metal atoms, copper in this case, can be locked in the vacancies as reduced forms. As the amount of gadolinium increased among the samples, the number of surface oxygen vacancies will increase following the bulk vacancy trend. Therefore, small copper atoms can possibly meet the surface oxygen vacancies and drop into vacancies. This phenomenon has been previously reported for a copper catalyst on a yttrium-stabilized zirconia support [70]. The relationship between the reduced copper species on the surface and the PROX activity will be discussed in the next section.

3.6 Catalytic Performance

3.6.1 Effect of Gadolinium Doping on the Complete CO PROX Performance

Figure 7 presents the CO conversion (A) and O_2 selectivity to CO_2 (B) for the complete CO PROX reaction on the prepared catalysts. The complete CO PROX environment contained 1.0% CO (by volume hereinafter), 1.0% O_2, 50% H_2, 15% CO_2, 10% H_2O and N_2 balance. The WGS reactor was normally placed immediately in front of the PROX reactor, and its tail gas contained considerable amounts of CO_2 and H_2O [71, 72]. Previous studies have also argued that the contents of CO_2 and H_2O inside the reactant hinder selective CO oxidation [73, 74]. Therefore, examining the CO PROX activity under the presence of CO_2 and H_2O is important. As presented in Fig. 7a, every profile has a similar conversion shape following the typical light-off curve for the complete CO PROX reaction on the copper–ceria catalytic system [14]. Every plot exhibits an increasing trend of CO conversion until reaching a maximum value. After the maximum conversion is achieved, a gradual decrease is observed because of hydrogen oxidation. The oxidation of hydrogen requires a higher temperature than CO oxidation due to the higher activation energy for the reaction [75].

The negative effect of the introduction of gadolinium into the ceria support on the PROX activity is clearly shown in Fig. 7a, as a shift toward higher reaction temperatures was observed. The temperature region for the maximum (T_{max}) and 50% (T_{50}) conversion both increased as the gadolinium doping ratio increased. This trend is also observed in Fig. 7b. The lowest light-off curve and selectivity plot were obtained from the sample without any gadolinium content, i.e., CuO/CeO_2. In terms of the maximum CO conversion rate, the CuO/CeO_2, $CuO/CG_{0.05}$, and $CuO/CG_{0.1}$ samples reached above 98% CO conversion at 140–150, 150–160 and 160–170 °C, respectively. However, the samples containing more than 13 at.% gadolinium in their support could not reach a CO conversion rate above 98%. For $CuO/CG_{0.35}$, the maximum CO conversion rate reached only 60% at 250 °C. This dramatic decrease in the catalytic activity due to gadolinium doping is also shown in Fig. 7b in terms of the CO_2 selectivity. Therefore, the introduction of aliovalent cations inside the ceria support, such as Gd^{3+} in this case, does not promote the CO PROX activity, rather this doping deteriorates the CO oxidation performance.

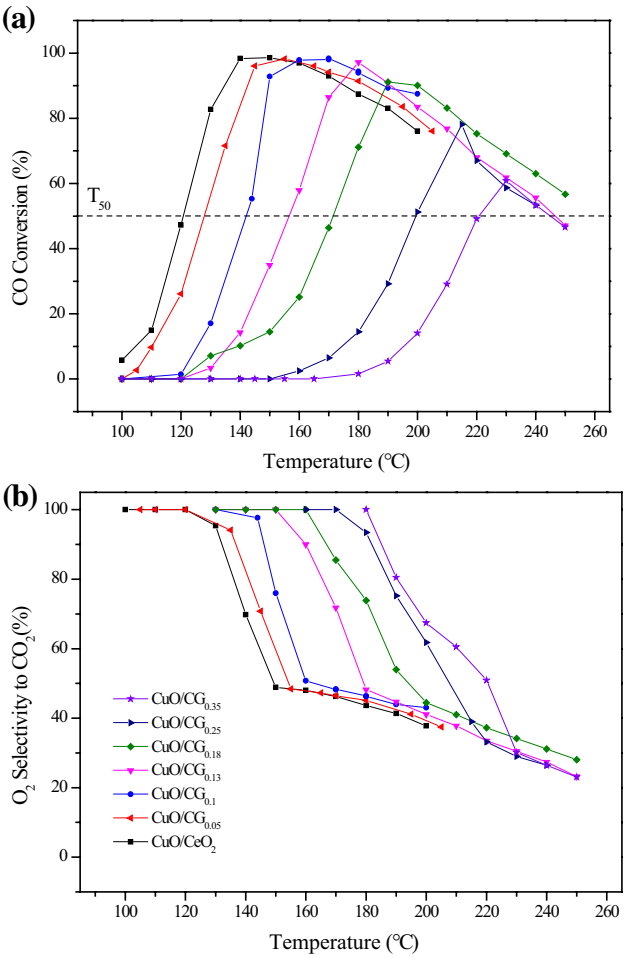

Fig. 7 **a** CO conversions as a function of temperature for (filled square) CuO/CeO_2, (filled left pointing triangle) $CuO/CG_{0.05}$, (filled circle) $CuO/CG_{0.1}$, (filled inverted triangle) $CuO/CG_{0.13}$, (filled diamond) $CuO/CG_{0.18}$, (filled right pointing triangle) $CuO/CG_{0.25}$ and (filled star) $CuO/CG_{0.35}$ under complete CO PROX conditions ($\lambda = 2$). **b** O_2 selectivities to CO_2 as a function of temperature under the same conditions

The effects of the gadolinium dopants on the physical and chemical characteristics of the catalysts were examined in the previous sections. The physical adsorption ability, which is determined by the S_{BET} and other pore values, did not considerably change among the samples. The dramatic change displayed on Fig. 7a likely cannot originate from the change of the physical adsorption ability by adding dopants. The crystallite size of the copper oxide detected on the XRD patterns decreased as the number of dopants increased. Normally, we can assume that the small size of the metal oxide species benefits the adsorption ability for CO oxidation, because the copper metal species are known as the

adsorption site for CO. However, the overall trend of Fig. 7a is in complete contrast to the trend of the copper oxide particle size. Therefore, we conclude that the CO adsorption, regardless of being a physical or chemical process, is not a rate-determining step for the CO PROX reaction on the copper–ceria system.

As the amount of gadolinium inside the ceria lattice increased, the bulk oxygen vacancies in the catalysts also increased, as shown by the structural analysis. The increment of the lattice strain, d-spacing and D band in the Raman spectra confirmed this well-known phenomenon. Thermodynamically, the number of surface oxygen vacancies changed with the number of bulk oxygen vacancies to maintain the defected structure of ceria [55]. Therefore, we can assume that a higher number of surface oxygen vacancies forms on the samples with a large amount of gadolinium, than the samples with a small amount of dopant. Based on the CO conversion trend in Fig. 7a, the surface oxygen vacancies do not help PROX on the catalysts. We can conclude that the extrinsic surface oxygen vacancies, generated by the artificial foreign dopants, may not actively participate in the CO PROX reaction. Still, there is a possibility that that the intrinsic surface oxygen vacancies, generated by the reducible Ce^{4+} ions, are beneficial for CO PROX.

The redox couple between copper and ceria described by Eq. (1) is well known as the essential equilibrium for the CO PROX reaction [48]. Based on the TPR results, various types of reducible copper species are observed for the samples containing small numbers of gadolinium dopants. However, as the amount of gadolinium increased, the number of types of reducible copper species decreased, and finally, only one single reduction peak was observed for the samples (f) and (g). This trend indicates that the interaction between copper and cerium by the exchange of oxygen or electrons is greatly decreased when non-reducible foreign dopants are inserted into the ceria lattice. The non-reducible intruders on the surface of ceria may hinder the metal–support interaction between copper and cerium. Consequently, the number of interacting species decreased, and separation between copper and ceria was observed. This trend was also confirmed by the Ce 3d XPS analysis. The relative ratio of Ce^{3+} gradually decreased when the doping ratio increased. This hindering effect by the dopants is clearly observed in Fig. 7a. Therefore, we conclude that the extent of the redox couple between the reducible copper and cerium is essential for the CO PROX activity even under the presence of CO_2 and H_2O.

Based on the surface analysis by XPS, two important characteristics were observed by analyzing the effect of the surface oxygen vacancies; "metal-burial" and "metal-nesting" effects [65]. These two characteristics related to copper on the surface of samples critically deteriorated the CO PROX activity. First, the absolute atomic amount of copper is diminished on the surface. In Table 4, the relative copper ratio on the analyzed area gradually decreased as the doping amount increased, indicating that the number of copper atoms compared to rare-earth elements decreased by an effect of the foreign dopants. Comparing the results of the bulk elemental analysis in Table 1, the absolute amounts of copper inside the catalysts are not changed, rather the surface copper species diminished when the doping ratio increased. This observation may correspond to the small copper atoms penetrating the surface of the gadolinium-doped ceria and burying inside the ceria lattice. Sanchez et al. explained that the surface oxygen vacancies can provide an open pathway for the penetration [65]. Therefore, we conclude that the absolute amount of exposed copper species on the surface decreased when the gadolinium doping ratio increased, affecting the final CO PROX activity of the catalyst. Second, stable, reduced copper species on the surface are not beneficial to the CO PROX activity. Based on the Cu 2p core level XPS spectra, the amount of Cu^{2+} species decreased and reduced copper species in the form of Cu^{+} or Cu^{0} increased. Dow et al. reported that small base-metal atoms, such as copper in this case, can be stored inside the surface oxygen vacancies via a phenomenon called the "metal-nesting" [65, 70]. During the XPS analysis, any pre-treatments, such as reduction at high temperature, were not performed. Therefore, "metal-nesting" is the only explanation for the increment of the reduced copper species over the oxidized species. Moreover, we can conclude that these stable reduced copper species are not beneficial to the CO PROX activity. Based on several previous reports, Cu^{+} species are considered chemisorption sites for CO oxidation [20, 48]. However, even if the reduced copper species serve as reaction sites for CO PROX, the mechanism proceeds when the reduced copper species are functional and highly interactive with the surrounded cerium atoms. Once the copper species are nested inside the surface oxygen vacancies in a stable form, re-oxidizing and extracting these species from the vacancies is difficult [65]. Therefore, the surface oxygen vacancies generated by the introduction of the foreign dopants are not beneficial and even deteriorate the CO PROX activity by forming nested copper species.

To compare the catalytic activities of the samples in different oxidation environments, complete CO PROX tests were conducted with varying λ values for selected samples. Figure 8a confirms that complete CO conversion is not fully accomplished in an oxygen deficient environment ($\lambda = 1$). However, in Fig. 8b, under oxygen sufficient conditions ($\lambda = 4$), the temperature range for 100% CO conversion increased for the $CuO/CG_{0.1}$ sample. These conversion profiles are consistent with typical mixed metal oxide catalysts according to the Mars-van Krevelen mechanism [19]. Although the amount of oxygen inside the reactant mixture was changed, the differences of the CO conversion ability between the samples were not affected. These results again

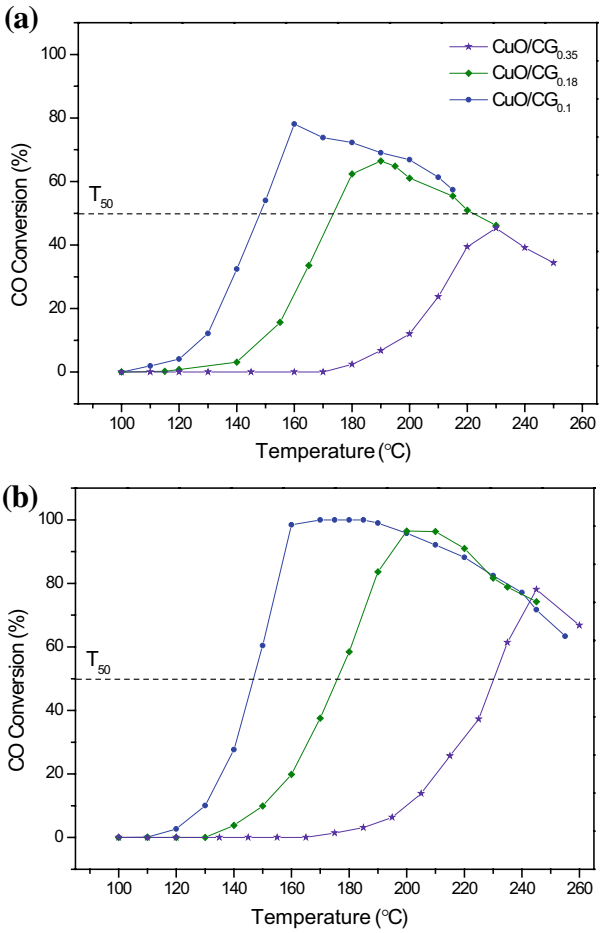

Fig. 8 **a** CO conversions as a function of temperature for (filled circle) $CuO/CG_{0.1}$, (filled diamond) $CuO/CG_{0.18}$ and (filled star) $CuO/CG_{0.35}$ under complete CO PROX conditions with deficient oxygen ($\lambda = 1$) and **b** sufficient oxygen ($\lambda = 4$)

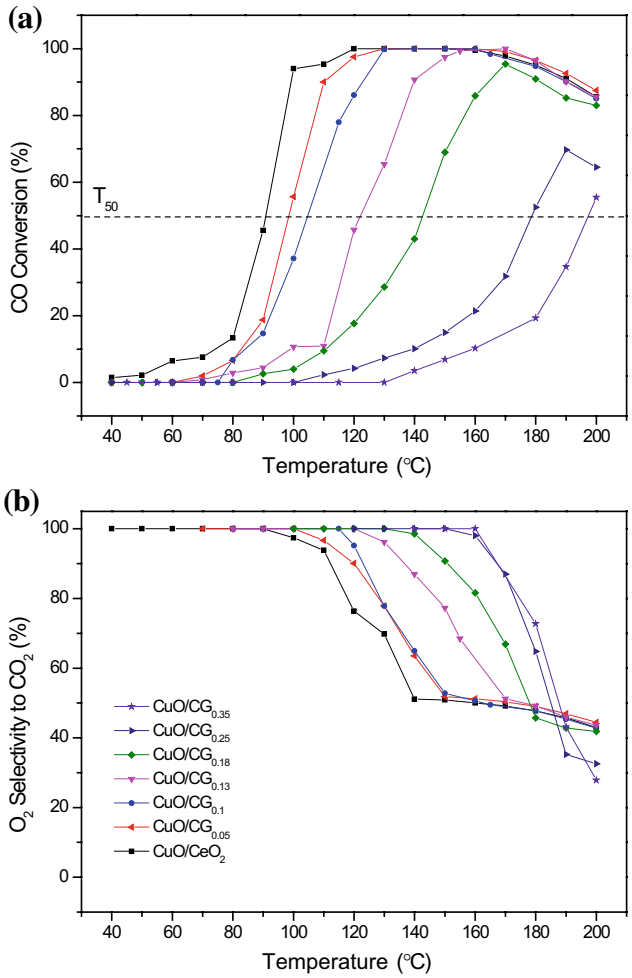

Fig. 9 **a** CO conversions as a function of temperature for (filled square) CuO/CeO, (filled left pointing triangle) $CuO/CG_{0.05}$, (filled circle) $CuO/CG_{0.1}$, (filled inverted triangle) $CuO/CG_{0.13}$, (filled diamond) $CuO/CG_{0.18}$, (filled right pointing triangle) $CuO/CG_{0.25}$ and (filled star) $CuO/CG_{0.35}$ under dry CO PROX conditions ($\lambda = 2$). **b** O_2 selectivities to CO_2 as a function of temperature under the same conditions

confirm that the negative effect of the introduction of gadolinium on the surface is strongly related to the surface redox couple and the amount and types of surface copper species.

3.6.2 *Effect of Gadolinium Doping on the Dry CO PROX Performance*

Figure 9a shows the CO conversion curves for the samples under dry CO PROX conditions, and Fig. 9b shows the O_2 selectivity to CO_2 under the same experiments. The dry CO PROX conditions consisted of the same reactant mixture excluding the moisture content. Normally, CO_2 and H_2O contents in the reactant mixture are considered hindrances for the CO PROX reaction. In particular, large amounts of absorbed molecular water have a blocking effect, preventing the reactants from accessing the catalytic active sites [73]. Compared with the results shown in Figs. 7a and 9a clearly shows that the hindrance from moisture is eliminated. The overall temperature region for the light-off curves decreased. The CuO/CeO_2 to $CuO/CG_{0.1}$ samples had relatively wide temperature windows for 100% CO conversion under these conditions. The windows for the samples were 120–160, 130–170 and 130–160 °C for CuO/CeO_2, $CuO/CG_{0.05}$ and $CuO/CG_{0.1}$, respectively. Moreover, $CuO/CG_{0.13}$ exhibited 100% CO conversion at 155–170 °C; however, this sample only reached 90% CO conversion under the complete CO PROX conditions. This overall enhanced catalytic trend indicates that CO oxidation occurred more easily in the dry environment without moisture, corresponding to the previously reported hindrance effect of H_2O. The selectivity trend in Fig. 9b is also consistent with the conversion data.

The negative effect of gadolinium doping on the CO conversion is also shown on the results obtained under the dry CO PROX experiments. As the doping amount increased,

the CO PROX activity decreased. This trend is also apparent in the selectivity plots. The discussion in the previous section comparing between the structural, redox, surface chemical properties, and CO PROX activity is apparently consistent with these experiments under dry conditions. Gamarra et al. reported that deactivation of the CuO/CeO_2 system for CO PROX by H_2O in the reactant mixture is based on the presence of undissociated water molecules on the surface in the low-temperature region [73]. Therefore, the negative effects from the dopant are also valid in the experiments under dry conditions after removing the blocking effect of the water molecules. Moreover, we may conclude that the surface oxygen vacancies generated by the dopants are not beneficial to remove moisture on the surface.

4 Conclusions

$CuO/Ce_{1-x}Gd_xO_{2-\delta}$ samples were synthesized using a combustion method and impregnation with various amounts of gadolinium to investigate the effect of dopants inside ceria on the CO PROX reaction. The physical, structural, redox and surface chemical properties of the catalysts were characterized by several analytical techniques. Negative effects of the gadolinium dopants inside the ceria lattice on CO PROX were found. Four considerable findings, based on the physical and chemical characterizations, related to the influence of the gadolinium dopants on the CO PROX activity were found. First, the adsorption ability of the catalyst was not significant to the CO PROX activity. The physical adsorption ability was controlled regardless of the number of gadolinium dopants; however, considerable differences between the CO conversion abilities among the samples were observed. Second, extrinsically generated surface oxygen vacancies were not beneficial to the CO PROX reaction. Although the CO PROX reaction followed the Mars-van Krevelen mechanism, the CO PROX activities were not promoted when the extrinsic oxygen vacancies increased. Third, the efficiency of the redox couple on the surface between copper and cerium was essential for the CO PROX activity. The presence of non-reducible gadolinium on the surface critically deteriorated the formation of Ce^{3+} and reducible copper species interacting with cerium on the surface, affecting to the CO PROX activities. Finally, the extrinsic surface oxygen vacancies consume the active copper species on the surface by burying and nesting. By surface analysis, the absolute number of copper species was shown to diminish, and the relative ratio of reduced copper species increased when the amount of gadolinium doping increased. These observations correspond to copper atoms on the surface penetrating through the surface oxygen vacancies and storing in the vacancies as a stable reduced form. Therefore, the surface oxygen vacancies do not promote the CO PROX reaction. Based on these four findings, we conclude that the introduction of foreign dopants, gadolinium in this case, has a negative effect on the CO PROX activity.

Acknowledgements This work was supported by the New & Renewable Energy Core Technology Program of the Korea Institute of Energy Technology Evaluation and Planning (KETEP) granted financial resource from the Ministry of Trade, Industry & Energy, Republic of Korea (No. 20153010031930). Also, this work was supported by the Global Frontier R&D Program on Center for Multiscale Energy System funded by the National Research Foundation under the Ministry of Science, ICT & Future, Korea (2011–0031569). Additionally, the authors with to thank Saudi Aramco, Saudi Arabia for the financial assistance and permission to publish results.

References

1. Ahmed S, Krumpelt M (2001) Hydrogen from hydrocarbon fuels for fuel cells. Int J Hydr Energy 26:291–301
2. Santacesaria E, Carrá S (1983) Kinetics of catalytic steam reforming of methanol in a cstr reactor. Appl Catal 5:345–358
3. Igarashi H, Fujino T, Watanabe M (1995) Hydrogen electrooxidation on platinum catalysts in the presence of trace carbon monoxide. J Electroanal Chem 391:119–123
4. Tanaka H, Kuriyama M, Ishida Y, Ito S-I, Tomishige K, Kunimori K (2008) Preferential CO oxidation in hydrogen-rich stream over Pt catalysts modified with alkali metals: part I. Catalytic performance. Appl Catal A 343:117–124
5. Pozdnyakova O, Teschner D, Wootsch A, Kröhnert J, Steinhauer B, Sauer H, Toth L, Jentoft FC, Knop-Gericke A, Paál Z, Schlögl R (2006) Preferential CO oxidation in hydrogen (PROX) on ceria-supported catalysts, part II: oxidation states and surface species on Pd/CeO_2 under reaction conditions, suggested reaction mechanism. J Catal 237:17–28
6. Wang L, Chen J, Patel A, Rudolph V, Zhu Z (2012) Catalytic performance of Ru nanoparticles supported on different mesoporous silicas for preferential oxidation of CO in H_2-rich atmosphere. Appl Catal A 447–448:200–209
7. Han YF, Kahlich MJ, Kinne M, Behm RJ (2004) CO removal from realistic methanol reformate via preferential oxidation—performance of a Rh/MgO catalyst and comparison to Ru/γ-Al_2O_3, and Pt/γ-Al_2O_3, Appl Catal B 50:209–218
8. Adlhart Otto J, Cohn Johann GE, Walter E, Straschil Heinrich K (1971) Process for oxidation of carbon monoxide. Google Patents
9. Kim YH, Park ED, Lee HC, Lee D, Lee KH (2009) Preferential CO oxidation over supported noble metal catalysts. Catal Today 146:253–259
10. Avgouropoulos G, Ioannides T (2003) Selective CO oxidation over $CuO–CeO_2$ catalysts prepared via the urea–nitrate combustion method. Appl Catal A 244:155–167
11. Costello CK, Kung MC, Oh HS, Wang Y, Kung HH (2002) Nature of the active site for CO oxidation on highly active Au/γ-Al_2O_3. Appl Catal A 232:159–168
12. Teng Y, Sakurai H, Ueda A, Kobayashi T (1999) Oxidative removal of co contained in hydrogen by using metal oxide catalysts. Int J Hydr Energy 24:355–358
13. Liu W, Flytzanistephanopoulos M (1995) Total oxidation of carbon monoxide and methane over transition metal fluorite oxide composite catalysts. J Catal 153:304–316

14. Liu Y, Fu Q, Stephanopoulos MF (2004) Preferential oxidation of CO in H_2 over CuO–CeO_2 catalysts. Catal Today 93–95:241–246
15. Guo Q, Liu Y (2008) MnO_x modified Co_3O_4-CeO_2 catalysts for the preferential oxidation of CO in H_2-rich gases. Appl Catal B 82:19–26
16. Kandoi S, Gokhale AA, Grabow LC, Dumesic JA, Mavrikakis M (2004) Why Au and Cu are more selective than Pt for preferential oxidation of CO at low temperature. Catal Lett 93:93–100
17. Wu Z, Zhu H, Qin Z, Wang H, Huang L, Wang J (2010) Preferential oxidation of CO in H_2-rich stream over CuO/$Ce_{1-x}Ti_xO_2$ catalysts. Appl Catal B 98:204–212
18. Liu W, Flytzanistephanopoulos M (1995) Total oxidation of carbon-monoxide and methane over transition metal fluorite oxide composite catalysts. J Catal 153:317–332
19. Sedmak G, Hočevar S, Levec J (2004) Transient kinetic model of CO oxidation over a nanostructured Cu0.1Ce0.9O_{2-y} catalyst. J Catal 222:87–99
20. Martínez-Arias A, Gamarra D, Hungría BA, Fernández-García M, Munuera G, Hornés A, Bera P, Conesa CJ, Cámara LA (2013) Characterization of active sites/entities and redox/catalytic correlations in copper–ceria-based catalysts for preferential oxidation of CO in H_2-rich streams. Catalysts 3(2):378–400
21. Sedmak G, Hočevar S, Levec J (2003) Kinetics of selective CO oxidation in excess of H_2 over the nanostructured Cu0.1Ce0.9O_{2-y} catalyst. J Catal 213:135–150
22. Wang JB, Lin S-C, Huang T-J (2002) Selective CO oxidation in rich hydrogen over CuO/samaria-doped ceria. Appl Catal A 232:107–120
23. Lin R, Luo M-F, Zhong Y-J, Yan Z-L, Liu G-Y, Liu W-P (2003) Comparative study of CuO/Ce0.7Sn0.3O_2, CuO/CeO_2 and CuO/SnO_2 catalysts for low-temperature CO oxidation. Appl Catal A 255:331–336
24. Chen Y-Z, Liaw B-J, Chang W-C, Huang C-T (2007) Selective oxidation of CO in excess hydrogen over catalysts. Int J Hydr Energy 32:4550–4558
25. Cecilia JA, Arango-Díaz A, Rico-Pérez V, Bueno-López A, Rodríguez-Castellón E (2015) The influence of promoters (Zr, La, Tb, Pr) on the catalytic performance of CuO–CeO_2 systems for the preferential oxidation of CO in the presence of CO_2 and H_2O. Catal Today 253:115–125
26. Ratnasamy P, Srinivas D, Satyanarayana CVV, Manikandan P, Senthil Kumaran RS, Sachin M, Shetti VN (2004) Influence of the support on the preferential oxidation of CO in hydrogen-rich steam reformates over the CuO–CeO_2–ZrO_2 system. J Catal 221:455–465
27. Ayastuy JL, Gurbani A, González-Marcos MP, Gutiérrez-Ortiz MA (2012) Selective CO oxidation in H_2 streams on CuO/$Ce_xZr_{1-x}O_2$ catalysts: correlation between activity and low temperature reducibility. Int J Hydr Energy 37:1993–2006
28. Martínez-Arias A, Hungría AB, Fernández-García M, Conesa JC, Munuera G (2005) Preferential oxidation of CO in a H_2-rich stream over CuO/CeO_2 and CuO/(Ce,M)O_x (M = Zr, Tb) catalysts. J Power Sources 151:32–42
29. Hennings U, Reimert R (2007) Noble metal catalysts supported on gadolinium doped ceria used for natural gas reforming in fuel cell applications. Appl Catal B 70:498–508
30. Hernández WY, Laguna OH, Centeno MA, Odriozola JA (2011) Structural and catalytic properties of lanthanide (La, Eu, Gd) doped ceria. J Solid State Chem 184:3014–3020
31. Colussi S, de Leitenburg C, Dolcetti G, Trovarelli A (2004) The role of rare earth oxides as promoters and stabilizers in combustion catalysts. J Alloys Compd 374:387–392
32. Lee S, Bae M, Bae J, Katikaneni SP (2015) Ni–Me/Ce0.9Gd0.1O_{2-x} (Me: Rh, Pt and Ru) catalysts for diesel prereforming. Int J Hydr Energy 40:3207–3216
33. Mosqueda B, Toyir J, Kaddouri A, Gélin P (2009) Steam reforming of methane under water deficient conditions over gadolinium-doped ceria. Appl Catal B 88:361–367
34. He D, Hao H, Chen D, Liu J, Yu J, Lu J, Liu F, Wan G, He S, Luo Y (2017) Synthesis and application of rare-earth elements (Gd, Sm, and Nd) doped ceria-based solid solutions for methyl mercaptan catalytic decomposition. Catal Today 281(Part 3):559–565
35. Marina OA, Bagger C, Primdahl S, Mogensen M (1999) A solid oxide fuel cell with a gadolinia-doped ceria anode: preparation and performance. Solid State Ionics 123:199–208
36. Andreeva D, Ivanov I, Ilieva L, Abrashev MV, Zanella R, Sobczak JW, Lisowski W, Kantcheva M, Avdeev G, Petrov K (2009) Gold catalysts supported on ceria doped by rare earth metals for water gas shift reaction: Influence of the preparation method. Appl Catal A 357:159–169
37. Ilieva L, Pantaleo G, Ivanov I, Zanella R, Venezia AM, Andreeva D (2009) A comparative study of differently prepared rare earths-modified ceria-supported gold catalysts for preferential oxidation of CO. Int J Hydr Energy 34:6505–6515
38. Purohit RD, Sharma BP, Pillai KT, Tyagi AK (2001) Ultrafine ceria powders via glycine-nitrate combustion. Mater Res Bull 36:2711–2721
39. Grazulis S, Chateigner D, Downs RT, Yokochi AFT, Quiros M, Lutterotti L, Manakova E, Butkus J, Moeck P, Le Bail A (2009) Crystallography open database: an open-access collection of crystal structures. J Appl Crystallogr 42:726–729
40. Lee HC, Kim DH (2008) Kinetics of CO and H_2 oxidation over CuO–CeO_2 catalyst in H_2 mixtures with CO_2 and H_2O. Catal Today 132:109–116
41. Holland B (2003) Determination of both mesopores and macropores in three-dimensional ordered porous materials by nitrogen adsorption. J Porous Mater 10:17–22
42. Hennings U, Reimert R (2007) Investigation of the structure and the redox behavior of gadolinium doped ceria to select a suitable composition for use as catalyst support in the steam reforming of natural gas. Appl Catal A 325:41–49
43. Hong SJ, Virkar AV (1995) Lattice parameters and densities of rare-earth oxide doped ceria electrolytes. J Am Ceram Soc 78:433–439
44. Shannon RD (1976) Revised effective ionic-radii and systematic studies of interatomic distances in halides and chalcogenides. Acta Crystallogr A 32:751–767
45. Zhou XD, Huebner W (2001) Size-induced lattice relaxation in CeO_2 nanoparticles. Appl Phys Lett 79:3512–3514
46. Halder NC, Wagner CNJ (1966) Separation of particle size and lattice strain in integral breadth measurements. Acta Crystallograph 20:312–313
47. Si R, Zhang Y-W, Li S-J, Lin B-X, Yan C-H (2004) Urea-based hydrothermally derived homogeneous nanostructured $Ce_{1-x}Zr_xO_2$ (x = 0–0.8) solid solutions: a strong correlation between oxygen storage capacity and lattice strain. J Phys Chem B 108:12481–12488
48. Gamarra D, Munuera G, Hungría AB, Fernández-García M, Conesa JC, Midgley PA, Wang XQ, Hanson JC, Rodríguez JA, Martínez-Arias A (2007) Structure–activity relationship in nanostructured copper–ceria-based preferential CO oxidation catalysts. J Phys Chem C 111:11026–11038
49. Mahata T, Das G, Mishra RK, Sharma BP (2005) Combustion synthesis of gadolinia doped ceria powder. J Alloys Compd 391:129–135
50. Sudarsanam P, Mallesham B, Reddy PS, Großmann D, Grünert W, Reddy BM (2014) Nano-Au/CeO_2 catalysts for CO oxidation: influence of dopants (Fe, La and Zr) on the physicochemical properties and catalytic activity. Appl Catal B 144:900–908
51. Taniguchi T, Watanabe T, Sugiyama N, Subramani AK, Wagata H, Matsushita N, Yoshimura M (2009) Identifying defects in

ceria-based nanocrystals by UV resonance Raman spectroscopy. J Phys Chem C 113:19789–19793
52. Weber WH, Hass KC, McBride JR (1993) Raman study of CeO_2: second-order scattering, lattice dynamics, and particle-size effects. Phys Rev B 48:178–185
53. Nakajima A, Yoshihara A, Ishigame M (1994) Defect-induced Raman spectra in doped CeO_2. Phys Rev B 50:13297–13307
54. Prasad DH, Park SY, Ji HI, Kim HR, Son JW, Kim BK, Lee HW, Lee JH (2012) Structural characterization and catalytic activity of $Ce0.65Zr0.25RE0.1O_{2-\delta}$ nanocrystalline powders synthesized by the glycine-nitrate process. J Phys Chem C 116:3467–3476
55. Trovarelli A (2002) Catalysis by ceria and related materials. Imperial College Press, London
56. Hegde MS, Madras G, Patil KC (2009) Noble metal ionic catalysts. Acc Chem Res 42:704–712
57. Konsolakis M, Ioakeimidis Z (2014) Surface/structure functionalization of copper-based catalysts by metal-support and/or metal–metal interactions. Appl Surf Sci 320:244–255
58. Zhu H, Qin Z, Shan W, Shen W, Wang J (2004) Pd/CeO_2–TiO_2 catalyst for CO oxidation at low temperature: a TPR study with H_2 and CO as reducing agents. J Catal 225:267–277
59. Zou H, Dong X, Lin W (2006) Selective CO oxidation in hydrogen-rich gas over CuO/CeO_2 catalysts. Appl Surf Sci 253:2893–2898
60. Ayastuy JL, Gurbani A, González-Marcos MP, Gutiérrez-Ortiz MA (2010) CO oxidation on $Ce_XZr_{1-X}O_2$-supported CuO catalysts: correlation between activity and support composition. Appl Catal A 387:119–128
61. Pintar A, Batista J, Hočevar S (2005) TPR, TPO, and TPD examinations of $Cu0.15Ce0.85O_{2-y}$ mixed oxides prepared by co-precipitation, by the sol–gel peroxide route, and by citric acid-assisted synthesis. J Colloid Interface Sci 285:218–231
62. Liu W, Flytzani-Stephanopoulos M (1996) Transition metal-promoted oxidation catalysis by fluorite oxides: a study of CO oxidation over $Cu{\cdot}CeO_2$. Chem Eng J Biochem Eng J 64:283–294
63. Kundakovic L, Flytzani-Stephanopoulos M (1998) Reduction characteristics of copper oxide in cerium and zirconium oxide systems., Appl Catal A 171:13–29
64. Luo M-F, Zhong Y-J, Yuan X-X, Zheng X-M (1997) TPR and TPD studies of $CuOCeO_2$ catalysts for low temperature CO oxidation. Appl Catal A 162:121–131
65. Sanchez MG, Gazquez JL (1987) Oxygen vacancy model in strong metal–support interaction. J Catal 104:120–135
66. Holmgren A, Azarnoush F, Fridell E (1999) Influence of pretreatment on the low-temperature activity of Pt/ceria. Appl Catal B 22:49–61
67. Kotani A, Jo T, Parlebas J (1988) Many-body effects in core-level spectroscopy of rare-earth compounds. Adv Phys 37:37–85
68. Avgouropoulos G, Ioannides T (2006) Effect of synthesis parameters on catalytic properties of CuO–CeO_2. Appl Catal B 67:1–11
69. Svintsitskiy DA, Kardash TY, Stonkus OA, Slavinskaya EM, Stadnichenko AI, Koscheev SV, Chupakhin AP, Boronin AI (2013) In situ XRD, XPS, TEM, and TPR Study of highly active in CO oxidation CuO nanopowders. J Phys Chem C 117:14588–14599
70. Dow WP, Huang TJ (1994) Effects of oxygen vacancy of Yttria-stabilized zirconia support on carbon monoxide oxidation over copper catalyst. J Catal 147:322–332
71. Choi Y, Stenger HG (2003) Water gas shift reaction kinetics and reactor modeling for fuel cell grade hydrogen. J Power Sources 124:432–439
72. Ahluwalia RK, Zhang Q, Chmielewski DJ, Lauzze KC, Inbody MA (2005) Performance of CO preferential oxidation reactor with noble-metal catalyst coated on ceramic monolith for on-board fuel processing applications. Catal Today 99:271–283
73. Gamarra D, Martinez-Arias A (2009) Preferential oxidation of CO in rich H-2 over CuO/CeO_2: operando-DRIFTS analysis of deactivating effect of CO_2 and H_2O. J Catal 263:189–195
74. Di Benedetto A, Landi G, Lisi L, Russo G (2013) Role of CO_2 on CO preferential oxidation over CuO/CeO_2 catalyst. Appl Catal B 142–143:169–177
75. Gawade P, Bayram B, Alexander A-MC, Ozkan US (2012) Preferential oxidation of CO (PROX) over CoO_x/CeO_2 in hydrogen-rich streams: effect of cobalt loading. Appl Catal B 128:21–30